Extension of the TraPPE force field for battery electrolyte solvents

Zhifen Luo,[†] Stephen A. Burrows,[‡] Stoyan K. Smoukov,[*,‡] Xiaoli Fan,[*,†] and Edo S. Boek[*,‡]

†*State Key Laboratory of Solidification Processing, School of Materials Science and Engineering, Northwestern Polytechnical University, 127 West Youyi Road, Xi'an Shaanxi, 710072, P.R.China*

‡*Chemical Engineering and Renewable Energy, School of Engineering and Materials Science, Queen Mary University of London, Mile End Road, London, E1 4NS, UK*

E-mail: s.smoukov@qmul.ac.uk; xlfan@nwpu.edu.cn; e.boek@qmul.ac.uk

Phone: +44 (0)20 7882 2964

Abstract

Optimizing electrolyte formulations is key to improving performance of Li/Na-ion batteries, where transport properties (diffusion coefficient, viscosity) and permittivity need to be predicted as functions of temperature, salt concentration and solvent composition. More efficient and reliable simulation models are urgently needed, owing to the high cost of experimental methods and the lack of united-atom molecular dynamics force fields validated for electrolyte solvents. Here the computationally efficient TraPPE united-atom force field is extended to be compatible with carbonate solvents, optimizing the charges and dihedral potential. Computing the properties of electrolyte solvents, ethylene carbonate (EC), propylene carbonate (PC), dimethyl carbonate (DMC), diethyl carbonate (DEC) and dimethoxyethane (DME), we observe that the average absolute error in the density, self-diffusion coefficient, permittivity, viscosity and surface tension is approximately 15% of the corresponding experimental values. Results compare favorably to all-atom CHARMM and OPLS-AA force fields, offering computational performance improvement of at least 80%. We further use TraPPE to predict the structure and properties of $LiPF_6$ salt in these solvents and their mixtures. EC and PC form complete solvation shells around Li^+ ions, while the salt in DMC forms chain-like structures. In the poorest solvent, DME, $LiPF_6$ forms globular clusters despite DME's higher permittivity than DMC.

Introduction

Lithium-ion batteries (LIBs)[1,2] are currently widely exploited for high-performance electrochemical energy storage. LIBs have largely revolutionized our modern life[3–5] and are widely applied in electric and hybrid vehicles.[6,7] However, the time required to recharge LIBs for vehicle applications is still a bottleneck. Just as important for meeting CO_2 reduction goals is utility-level battery storage, to smoothen the energy supply from intermittent renewables (solar, wind), with both high capacity and power. The Hornsdale Power Reserve in Australia delivering 150 MW (194 MWh) is an undeniable success and utility battery storage is set for

rapid growth.[8] Current technologies and costs are available at NREL's Annual Technology Baseline (ATB),[9] but the development of better LIBs and future sodium ion batteries with higher energy and power density as well as shorter recharging times are essential to improving our daily lives, especially for the widespread adoption of electric vehicles and utility storage. We briefly describe the structure of the batteries to highlight current challenges.

An LIB cell consists of two porous electrodes and an electrolyte. The two electrodes, normally a graphite anode and a transition metal oxide cathode,[10–12] provide the host materials for Li^+ intercalation. The electrolyte is usually composed of lithium salt dissolved in an ion-conductive solvent and acts as a separator to keep the two electrodes apart. The performance of LIBs depends strongly on the combination of the electrodes, salt and solvent.[2] The standard salt commonly used in Li^+ ion batteries is $LiPF_6$.

In LIBs, the electrolyte solution usually consists of high-permittivity cyclic carbonates including ethylene carbonate (EC) and propylene carbonate (PC), mixed with linear carbonates, such as dimethyl carbonate (DMC), diethyl carbonate (DEC) and ethyl methyl carbonate (EMC).[13] The choice of solvent is an important determining factor in the performance of the lithium-ion battery.[14,15] Specifically, a good solvent prevents the formation of ion-ion pairs as they reduce the number of free charge-carrying ions, negatively affecting the conductivity.[15] The ionic conductivity and transport properties of Li^+ ions are affected not only by the properties of the solvent alone, but they also change significantly as a function of salt activity. Hence salt and solvent choice are important to the overall performance, ageing and safety of the LIB[16] and the effect of the electrolyte composition on the physical properties of the solution, Li^+ diffusion coefficient and conductivity all need to be understood.

Commonly used methods to investigate the structure of the electrolyte and interactions of dissolved salt ions with solvent molecules include neutron diffraction measurements,[17,18] nuclear magnetic resonance (NMR)[19–26] and vibrational spectroscopies (infrared (IR) spectroscopy and Raman scattering)[18,19,22,24,27,28] as well as computational methods: quantum chemical calculations[29,30] and molecular dynamics (MD) simulations.[31–34]

Neutron diffraction has been used to determine the coordination number and nearest neighbor distance of Li^+ to the carbonyl oxygen in EC solvent.[18] Neutron scattering experiments require synchrotron radiation facilities and therefore are not widely available. NMR is a commonly used method to accurately measure the diffusion coefficient of electrolyte components.[20] For vibrational spectroscopies, the wide variety of sample types, smaller sample requirement and fast analysis have enabled their widespread usage in structure and composition analysis.[35] Raman spectroscopy has been used to determine conformer populations in 1,2-dimethoxyethane (DME),[36,37] a widely used low-permittivity solvent in electrolytes. However, Raman may not be appropriate for all samples, as there are not only limitations due to sensitivity and absorption, but also the issue of fluorescent emission of photons which interferes with the spectra from Raman scattering. This can be mitigated by using near-IR excitation, since the near-IR photons usually do not have enough energy to induce the excited states that cause fluorescence (Ref.[35] p. 32).

At a typical salt concentration of 1 mol/L (1M), the number of Li^+ ions and counterions is at least one order of magnitude less than the number of solvent molecules. Hence the total number of molecules in the simulated electrolyte system must be at least thousands to obtain reasonable statistics for ionic properties. Larger systems are also desirable to mitigate finite-size effects associated with diffusion coefficient measurements.[38] Because of the high computational cost of quantum chemistry simulations for systems of this size, MD simulation becomes the most viable choice to investigate the electrolyte properties. It can reproduce properties at conditions (e.g. temperature and pressure) difficult to access in experiment. By analyzing the coordination structure, MD simulation can also study the mechanism of Li^+ diffusion. Carrier diffusion implies complete surrounding of Li^+ by its solvent shell which diffuses as a unit, whereas jump diffusion involves hopping of Li^+ between solvent molecules.[15]

An ideal solvent should have a high polarity (relative permittivity $\epsilon > 15$) in order to enable the full dissolution of the salt, since it can screen the ionic charges and decrease the

attractive interactions between cations and anions more effectively. A low viscosity is also desirable to improve the mobility of Li^+ ions, as is a wide operating temperature range[39,40] and good safety profile such as high auto-ignition and flash point temperatures.[41] Cyclic carbonates such as EC and PC are examples of aprotic solvents with high stability within a broad operating temperature range. Ethylene carbonate is the most widely used electrolyte solvent in LIBs because of its high relative permittivity of 90.5[42,43] so that the salt will be well dispersed. The presence of EC and PF_6^-, the typical counterion of Li^+, supports the formation of a stable solid electrolyte interface (SEI)[44] on the surface of graphite. The main disadvantage of EC by itself is its somewhat higher viscosity, but it can achieve high ionic conductivity when mixed with low-permittivity additives, further increasing the performance.[45] Another common high-permittivity solvent is PC, with a high dielectric constant of 64.92, but also high viscosity of 2.53 cP at 25 °C.[46] Therefore, a suitable choice for formulating electrolytes will typically combine high-permittivity cyclic carbonates with low-viscosity linear carbonates, achieving optimal performance in LIBs.

The OPLS-AA force field[47] has been optimized over many years for the simulation of liquids, using all-atom (AA) potentials. You *et al.* applied the OPLS-AA force field to EC and PC, investigating the dielectric constants, relaxation times and molecular mobilities.[48] The CHARMM all-atom force field[49,50] is widely used for MD studies of biomolecules in particular, and the SwissParam tool also allows CHARMM input files to be generated for small organic molecules such as electrolyte solvents.[51] Caleman *et al.*[52] performed benchmark simulations for 146 organic liquids to compute their density, heat of vaporization, surface tension, compressibility, relative permittivity and more, using OPLS-AA, generalized Amber force field (GAFF) and CHARMM. The results obtained for OPLS-AA and CHARMM appeared to be slightly better than GAFF for small organic molecules. Nunez *et al.*[53] used the united-atom version of the Transferable Potentials for Phase Equilibria force field (TraPPE) to measure properties of 41 polar liquids, and discovered that the relative permittivity was typically underestimated but found a good overall level of accuracy for the density, heat of

vaporization and surface tension.

Force fields derived from OPLS-AA have been found to underestimate diffusion coefficients of both pure carbonate solvents[48] and $LiPF_6$ in solution.[54] The many-body polarizable model of Borodin and Smith[55] performs well, but is significantly more computationally expensive and the parameters are not publicly available. Chaudhari *et al.*[56] reported that rescaling the charges of electrolyte solvent molecules in the OPLS-AA force field can achieve optimization of $LiPF_6$ diffusion coefficients. However, they did not find a constant rescaling factor that worked well for all molecules, recommending factors of 80%, 90% and 100% for EC, PC and $LiPF_6$, respectively. Earlier, a similar approach was applied to ionic liquids by Chaban.[57] Karatrantos *et al.*[34] achieved excellent prediction of PC, Li^+ and PF_6^- diffusion coefficients using the GAFF force field with PC charges scaled by 90% and ions by 85%.

In this work, we extend the computationally efficient united-atom TraPPE force field to support carbonate solvents, optimizing point charges for EC, PC, DMC, DEC and DME. We note that DME is a linear ether rather than a carbonate and is already supported by TraPPE, but is included due to its wide use in LIBs. We measure the density, self-diffusion coefficient, permittivity, surface tension and viscosity of some representative pure and mixed electrolyte solvent systems using the newly optimized TraPPE parameters. Using the OPLS-AA and CHARMM force fields as MD benchmarks, we compare the newly optimized TraPPE potential results with the corresponding experimental ones. We focus on lithium cation electrolytes with a hexafluorophosphate (PF_6^-) counter ion, which is the most common choice of anion for Li-ion batteries.[46]

Methods

Software and Force Field

GROMACS[58,59] version 2019.3, compiled in single precision, was used for all MD simulations in this work. Simulations were executed on Intel Xeon Gold 6248 CPUs.

The TraPPE[60] united-atom force field was used as the foundation to develop an efficient MD model for electrolyte solvents. Suitable Lennard-Jones (LJ) parameters for carbonate solvents were chosen by identifying the most similar atom types from the ether,[60] acrylate[61] and cyclic ether[62] force fields. The LJ parameters chosen are reported alongside the corresponding optimized charges in the Results section.

The TraPPE models for glycols[60] and acrylates[61] include intramolecular 1-4 Coulomb interactions (for atoms separated by three bonds) but scaled by a factor of 0.5, with 1-4 LJ interactions excluded. This convention is also adopted in this work. The LJ potential was truncated using a 1.4 nm cutoff and the LJ tail correction to energy and pressure was used (DispCorr = EnerPres within the GROMACS .mdp file). All bond lengths were constrained, as is standard for TraPPE, which was done using the LINCS algorithm.[63]

LJ and charge parameters for $LiPF_6$ are taken from OPLS-AA,[64] and are also used by the Lopes and Padua ionic liquid force field.[65] These parameters are provided in Supporting Information Table S1.

The optimization scheme described in this work follows that of Burrows,[66] in which TraPPE dihedral (torsion) potentials for EC, PC, DMC and DME were fit to two-dimensional potential energy surfaces (PES). We use these dihedral potentials unmodified in this work. A description of the optimization algorithm and contour plots of the PES are provided in the Supporting Information, as are complete force field files for our GROMACS implementation. The overall strategy for the optimization is illustrated in Figure 1.

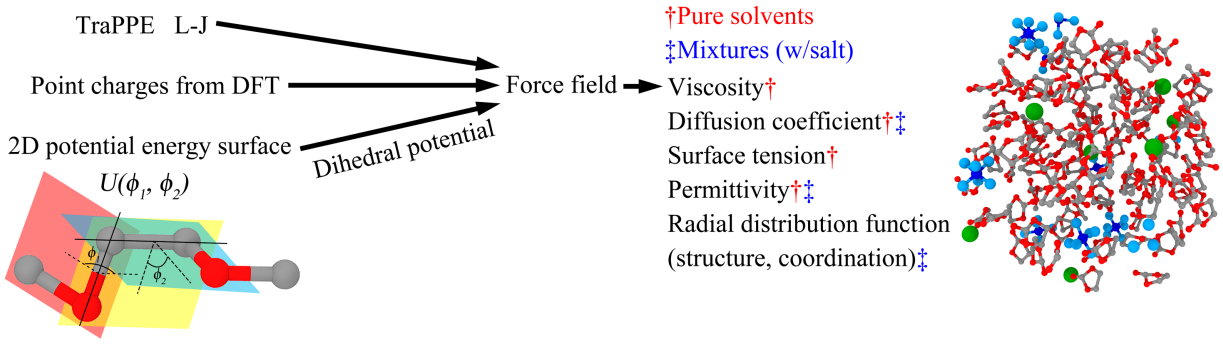

Figure 1: The overall strategy used to extend the TraPPE force field in this work.

Charge Optimization

To calculate point charges for the new molecules, density functional theory (DFT) calculations were performed using the B3LYP hybrid functional[67–69] with Grimme dispersion correction D3[70] and the aug-cc-pvtz basis set.[71,72] The NWChem software[73] was used for all DFT calculations. The electrostatic potential (ESP) fitting module was used to obtain charges which best reproduce the ESP around the molecule. As this is a united-atom model, the charges on all hydrogen atoms were constrained to zero so that point charges are optimized at the united-atom sites only. The grid points at which the ESP is computed are located in an envelope surrounding the molecule, defined by the region outside the probe radius r_p but within the cutoff distance r_{max} from the nuclei positions. Therefore, reducing the r_p value means this envelope approaches the nuclei more closely. However, since the purpose of the charges is to model intermolecular Coulomb interactions, fitting the ESP very close to the nucleus is less important. In this work, a range of r_p values are tested from 0.05 to 0.10 nm, with NWChem suggesting a default value of 0.07 nm. r_{max} was set to the default value of 0.3 nm. The ESP grid spacing was set to 0.01 nm.

Simulation Setup

All simulations of liquids begin with energy minimization followed by a 4 ns equilibration phase in the NPT ensemble using the Berendsen barostat[74] with a time constant of 1 ps and compressibility of 5×10^{-5} bar^{-1}. After this, a 12 ns NPT data collection simulation is carried out using the Parrinello-Rahman barostat.[75] The Bussi-Donadio-Parrinello thermostat,[76] denoted v-rescale in GROMACS, was used to control the temperature in all simulations with a time constant of 0.1 ps. The number of molecules was chosen to target a cubic simulation box size of ≈ 8 nm, and the system used periodic boundary conditions with the Ewald summation for long-range electrostatics.

For all reported properties, we obtain results averaged over 5 independent runs, each with a different random seed to generate the initial atom velocities at the start of the equilibration

phase. In order to match the temperature used in the diffusion experiments by Hayamizu *et al.*,[20] simulations of pure PC, DMC and DME were performed at 303 K, with 313 K being used for EC due to its higher melting point. Simulations of electrolyte systems with salt were performed at 298 K. The pressure was set to 1 bar for all systems. Systems containing salt used a 1M (1 mol/L) concentration of $LiPF_6$. The number of solvent and salt molecules for each system is tabulated in the Supporting Information.

Property Measurement

Diffusion Coefficient

The diffusion coefficient was computed from the mean squared displacement (MSD = $\langle|\mathbf{r}_i(t)-\mathbf{r}_i(0)|^2\rangle$), using the Einstein relation

$$D = \frac{1}{6}\lim_{t\to\infty}\frac{\mathrm{MSD}(t)}{t}\ , \tag{1}$$

where D is the self-diffusion coefficient, $\mathbf{r}_i(t)$ is the position vector of atom i at time t, and $\langle\rangle$ represents the average over all atoms. The MSD was obtained from the 12 ns NPT simulation by a linear fit. The finite-size correction of Yeh and Hummer[38] was applied to the self-diffusion coefficients measured for pure solvents,

$$D_0 = D_{PBC} + \frac{2.8373 k_B T}{6\pi\eta L} \tag{2}$$

where D_0 is the corrected value, D_{PBC} is the value measured by mean squared displacement in a periodic box of length L, and the viscosity η was computed as described below. This correction was not applied to compute diffusion coefficients of systems containing salt, as it was validated for single-component Newtonian fluids.

Relative Permittivity

The relative permittivity, ε, was calculated from fluctuations of the total dipole moment of the system using the GROMACS tool *gmx dipoles*, which uses the formula[77–79]

$$\varepsilon = 1 + \frac{\langle M^2 \rangle - \langle M \rangle^2}{3\varepsilon_0 V k_B T} \ , \tag{3}$$

where ε_0 is the vacuum permittivity, V is the volume of the simulation box, T is the constant simulation temperature, k_B is the Boltzmann constant, M denotes the total dipole moment of the simulation box, and $\langle\rangle$ represents the time average.

Surface Tension

The surface tension, γ, is derived from the difference in average pressure between the z direction, which is normal to the interface, and the in-plane x and y directions. GROMACS obtains the average pressure components by integration, and therefore γ is defined as[80]

$$\gamma = \frac{1}{n} \int_0^{L_Z} \left[P_{ZZ}(z) - \frac{1}{2} \left(P_{XX}(z) + P_{YY}(z) \right) \right] \mathrm{d}z \ , \tag{4}$$

where L_Z is the length of the simulation cell in the z direction, and P_{XX}, P_{YY} and P_{ZZ} are the three pressure components along the x, y and z directions, respectively. n is the number of interfaces which is two in our periodic system. In this work, an equilibrated NPT system with isotropic pressure coupling was taken to get the starting configuration for the liquid phase region. Then, we enlarged the simulation box by a factor of three in the z direction to create the interface, and the simulation was performed in the NVT ensemble to obtain the vapor-liquid surface tension. For surface tension measurements only, the LJ cutoff was increased to 2.5 nm to mitigate truncation effects.[81]

Viscosity

The viscosity can be calculated from a non-equilibrium simulation using the cosine-acceleration method.[82] In this approach, a spatially varying acceleration is applied to the atoms, with the following cosine form

$$a_x(z) = A\cos\left(\frac{2\pi z}{L_z}\right) \ , \tag{5}$$

where A is a parameter which specifies the maximum acceleration. Assuming a Newtonian fluid, the generated velocity profile $v_x(z)$ will have the form

$$v_x(z) = V\cos\left(\frac{2\pi z}{L_z}\right) \ . \tag{6}$$

After fitting this cosine velocity profile and obtaining the maximum velocity V, the viscosity is computed from A and V by

$$\eta = \frac{A}{V}\rho\left(\frac{L_z}{2\pi}\right)^2 \ , \tag{7}$$

where A is the cos-acceleration parameter in the GROMACS .mdp file. In Supporting Figure S5, the calculated viscosity is presented as a function of A. We see the viscosity decreases as A increases, which corresponds to increasing shear rate. Based on the extrapolation shown in Fig. S1, a cos-acceleration parameter of $A = 0.003$ nm/ps^2 results in a computed viscosity close to the zero shear rate result obtained by extrapolation to $A = 0$. Therefore this value was chosen for all the solvents when measuring viscosity.

Coordination Number

The radial distribution function (RDF) provides a basis for short-range structure analysis at the atomic level. It is a measure of the probability of finding particles of type j around particles type of i at distance r.

The RDF was determined by calculating the distance between all pairs of particles i and j then producing a histogram of these values. The histogram is then normalized with respect

to the number density of the type j particles, ρ_j, multiplied by the volume of the spherical shell between radii r and $r + \mathrm{d}r$, which can be expressed as $\rho_j 4\pi r^2 \mathrm{d}r$ where $\mathrm{d}r$ is the size of the histogram bin. The RDF, $g_{ij}(r)$, is therefore given by

$$g_{ij}(r) = \frac{\mathrm{d}n_j(r)}{\rho_j 4\pi r^2 \mathrm{d}r} \ , \tag{8}$$

where $\mathrm{d}n_j(r)$ is the mean number of type j particles in a shell at r of width $\mathrm{d}r$.

The coordination number $N(r_c)$ is calculated from the RDF, as

$$N(r_c) = \int_0^{r_c} 4\pi r^2 \rho_j g_{ij}(r) \mathrm{d}r \ , \tag{9}$$

where $g_{ij}(r)$ is the RDF for particles of type i and j, and ρ_j is the average number density of type j particles. Integrating up to a cutoff, which in this work was set to $r_c = 4.5$ Å, yields the average number of type j particles in the first coordination shell around type i.

DMC Conformers

DMC has two stable conformers with a large energy barrier separating them, and may therefore require long simulation times to reach the equilibrium distribution. To investigate this, we perform simulations with DMC starting in each of these conformers, denoted str1 (cis-cis) and str2 (cis-trans), as shown in Supplementary Figure S6. In str1, both O=C-O-CH_3 dihedrals are in the cis conformation. We use the time evolution of the RDF for the distance between atoms O1 and C5/C6 to check the final equilibration time, since the O1-C5/C6 interatomic distance varies between the two conformers. After 14 ns of simulation starting from str1, only a very small peak appears corresponding to the O1-C5/C6 distance of str2 at 0.34 nm, indicating the vast majority of the molecules remain in str1. When starting with all molecules in str2, we observe the peak corresponding to str2 decreasing continually and still decreasing at the end of a 24 ns simulation. These results suggest str1 has significantly lower energy than str2. Hence, we carried out DFT energy calculations of the

two conformers to confirm this and to estimate their populations, using the same functional and basis set as described in the Charge Optimization section above. The equilibrium fraction of str1 was estimated by

$$F_1 = \frac{e^{\frac{-U_1}{kT}}}{e^{\frac{-U_1}{kT}} + e^{\frac{-U_2}{kT}}} = \frac{e^{\frac{U_2-U_1}{kT}}}{e^{\frac{U_2-U_1}{kT}} + 1} \tag{10}$$

where F_1 is the fraction of str1; U_1 and U_2 are the energies of str1 and str2, respectively. We find the energy difference $U_2 - U_1$ to have a value of 11.829 kJ/mol, resulting in the estimated fraction of conformer str1 being approximately 0.99, which defines the starting ratio of conformers used in DMC simulations. However, this can only be taken as a guideline since the DFT energy computation is performed in vacuum and ignores intermolecular effects which may stabilize certain conformers. Previous estimates of the str1 population are in the range 0.94-0.98.[83,84]

Results and Discussion

Force Field Optimization and Pure Solvent Properties

Firstly, NWChem[73] was used to optimize the atomic charges for the molecules EC, PC, DME, DMC and DEC. Figure 2 shows the chemical structure of these five solvents with atom numbers. In Figure S7, the optimized charges for different values of r_p are reported to illustrate the sensitivity of the charges to this variable. The definition of r_p and the DFT settings are explained in the Charge Optimization section above. As expected, the oxygen atoms are assigned negative charges, with the carbonyl oxygen (O1) charge being largest in magnitude. The absolute charges of double-bonded O1 and the connected C2 atoms decrease as the parameter r_p is increased from 0.05 to 0.1 nm for EC, PC, DMC and DEC. However, for the DME solvent, the point charges of the terminal C1/C6 atoms are observed to increase, while the charges of central C3/C4 atoms decrease, as the r_p value is increased.

Then we used the TraPPE force field with different candidate sets of atomic charges

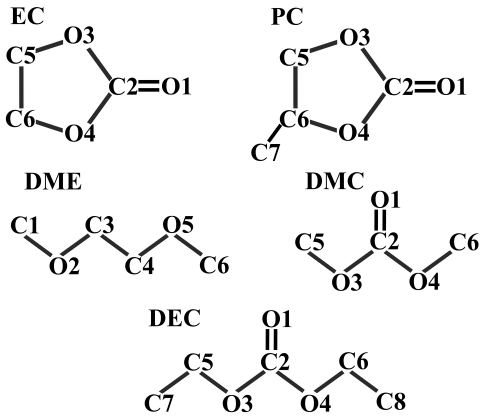

Figure 2: Chemical structures of electrolyte solvents with abbreviations and atom numbers.

(corresponding to different values of r_p), alongside the all-atom force field CHARMM, to measure the self-diffusion coefficient and relative permittivity of pure EC, PC, DMC, DEC and DME solvents. Input files for the CHARMM all-atom force field were generated using the SwissParam tool[51] (denoted CHARMM-SP) which is designed for small organic molecules. The dependence of self-diffusion coefficients and relative permittivities of the pure liquids EC, PC, DMC and DEC on r_p are presented in Supplementary Figures S8-9. All-atom OPLS-AA results for the diffusion coefficient and relative permittivity of EC and PC were obtained by You et al.,[48] and are used as an additional benchmark for those molecules.

Using the data in Figures S8-9, we compare the predictions of the self-diffusion coefficient and relative permittivity to choose the most suitable atomic charges for the extended TraPPE force field. The charge set corresponding to $r_p = 0.08$ had the highest level of accuracy in predicting the diffusion coefficient of the carbonate solvents (EC, PC and DMC) after applying the finite size correction proposed by Yeh and Hummer *et al.*[38] As we prioritize transport properties, we select this charge set. However, slightly more accurate prediction of relative permittivity was obtained using $r_p = 0.1$. The numerical values of the selected charges, computed with $r_p = 0.08$, are reported in Table 1 alongside the corresponding LJ parameters. The same parameters using TraPPE's standard units of Å and K are provided in the Supporting Information Table S2.

The diffusion coefficients predicted by the TraPPE potential for the carbonate solvents

Table 1: LJ parameters from the TraPPE force field[60–62] and newly optimized charges, where σ and ϵ are the LJ size parameter and well depth, respectively.

Molecule	Atom	σ (nm)	ϵ (kJ/mol)	Charge (|e|)
EC	O1	0.305	0.6568	-0.547
	C2	0.382	0.3326	0.825
	O3, O4†	0.220	1.5797	-0.399
	C5, C6 (CH_2)†	0.388	0.4681	0.260
PC	O1	0.305	0.6568	-0.547
	C2	0.382	0.3326	0.825
	O3, O4†	0.220	1.5797	-0.399
	C5 (CH_2)†	0.388	0.4681	0.260
	C6 (CH)	0.433	0.0831	0.260
	C7 (CH_3)	0.375	0.8148	0.0
DMC	O1	0.305	0.6568	-0.614
	C2	0.382	0.3326	0.932
	O3, O4	0.280	0.4573	-0.448
	C5, C6 (CH_3)	0.375	0.8148	0.289
DEC	O1	0.305	0.6568	-0.614
	C2	0.382	0.3326	0.932
	O3, O4	0.280	0.4573	-0.448
	C5, C6 (CH_2)	0.395	0.3825	0.289
	C7, C8 (CH_3)	0.375	0.8148	0.0
DME	C1, C6 (CH_3)	0.375	0.8148	0.204
	O2, O5	0.280	0.4573	-0.428
	C3, C4 (CH_2)	0.395	0.3825	0.224

†LJ parameters from Ref.[62] (5-membered cyclic ether). Others from Ref.[60,61]

are more accurate than those of CHARMM-SP, but for DME, the CHARMM-SP results are closer to the experimental values. We also compare the DME results to those using default TraPPE charges, in which oxygen and carbon have charges of -0.5 |e| and 0.25 |e|, respectively, finding the default force field more accurately reproduces the diffusion coefficient at the cost of a significant error in the relative permittivity. In addition, please note recent reparametrization of the TraPPE-UA model for oligoethers[85] recommending a partial charge of -0.44 for the ether oxygen, i.e., closer to the charge of -0.4278 obtained in the current work. We provide both versions of the DME model in the supporting input files.

The computed relative permittivity, ε, is shown in Table 2, with the dependence on r_p shown in Supporting Figure S9. We find that the TraPPE force field results of PC and DME correspond well to the experimental data. All force fields show some inaccuracy in reproducing ϵ for EC, with TraPPE and OPLS-AA overestimating ϵ by $\approx 30\%$ and CHARMM-SP underestimating by $\approx 22\%$. As for DMC, the relative permittivity calculated via the TraPPE and CHARMM-SP potential are both approximately 50% below the experimental value, with TraPPE being slightly more accurate. The DMC solvent has two possible conformers, each with a different dipole moment, and therefore the ratio of these two conformers may influence the measured permittivity. The cis-trans conformer, denoted str2 in Figure S6, has a larger dipole moment[83] and therefore the underestimation of ε may arise from an underestimation of this conformer's population.

To further validate the force field, we calculate the density, liquid-vapor surface tension and viscosity of pure EC, PC, DMC and DME solvents with the TraPPE force field using the parameters given in Table 1 and compare with the corresponding experimental values. The results are shown in Table 2. All the density results agree with the experimental data well, as the errors are all $\leq 3\%$. The viscosity prediction for EC, PC, DMC and DEC agrees well with the corresponding experimental values, with their errors all less than 6% in magnitude. The surface tension of the carbonate solvents is generally overestimated, by factors of 9% to 24%. For DME, we find the surface tension is reproduced to within 12% of the experimental

Table 2: Computed density (ρ), diffusion coefficient (D), relative permittivity (ε), surface tension (γ) and viscosity (η) of EC (313 K), PC (303 K), DMC (303 K), DEC (298K) and DME (303 K) using the TraPPE force field.

	solvent	computed value ± SD	experimental data	relative errors[†] (%)
ρ (g/cc)	EC	1.330[*]	1.323[a]	0.49
	PC	1.219	1.200[b]	1.56
	DMC	1.064	1.063[b]	0.04
	DEC	0.973	0.980[c]	-0.71
	DME	0.834	0.860[b]	-3.02
	DME def-q[‡]	0.863	0.860[b]	0.35
D (10^{-10} m^2/s)	EC	7.996 ± 0.135	8.00[d]	-0.05
	PC	5.886 ± 0.073	5.80[d]	1.48
	DMC	25.918 ± 0.457	26.00[d]	-0.32
	DEC	23.360 ± 0.457	-	-
	DME	51.217 ± 1.214	31.00[d]	65.22
	DME def-q[‡]	41.438 ± 1.413	31.00[d]	33.67
ε	EC	118.546 ± 3.550	89.00[e]	33.20
	PC	77.272 ± 7.53	64.90[f]	19.06
	DMC	1.616 ± 0.034	3.1[f]	-47.87
	DEC	1.372 ± 0.020	2.80[c]	-50.99
	DME	8.641 ± 0.202	7.20[f]	20.02
	DME def-q[‡]	14.405 ± 0.149	7.20[f]	100.00
γ (mN/m)	EC	62.527 ± 2.036	50.60[a]	23.57
	PC	48.277 ± 1.167	40.5[j]	19.20
	DMC	34.278 ± 0.826	29.90[g]	14.64
	DEC	28.676 ± 0.465	26.3[h]	9.03
	DME	21.631 ± 0.967	24.70[h]	-12.43
	DME def-q[‡]	25.167 ± 0.837	24.70[h]	1.89
η (mPa s)	EC	1.873 ± 0.066	1.90[a]	-1.41
	PC	2.496 ± 0.136	2.53[b]	-1.34
	DMC	0.603 ± 0.014	0.59[b]	5.81
	DEC	0.575 ± 0.019	0.61[c]	-5.70
	DME	0.263 ± 0.016	0.39[i]	-32.54
	DME def-q[‡]	0.350 ± 0.004	0.39[i]	-10.18

Experimental data: [a]from Ref.[86] , [b]Ref.[46] , [c]Ref.[87] , [d]Ref.[20] , [e]Ref.[86] , [f]Ref.[46] , [g]Ref.[88] , [h]Ref.[89] , [i]Ref.[90] , [j]Ref.[91] (25 °C)

[*]For ρ, all standard deviations (SD) are $< 10^{-4}$ g/cc and therefore not shown.

[†]Relative errors are in comparison to experimental values.

[‡]def-q refers to using default TraPPE charges (q_O = -0.5, q_C = 0.25 |e|) with the newly optimized dihedral potentials.

value and only 2% when using the default charges. However, the error in the computed viscosity of DME is close to -33%.

The results in Table 2 show the default TraPPE charges of DME, which better reproduce the diffusion coefficient, are also better suited to reproduce DME's viscosity (and surface tension). This is consistent with the Stokes–Einstein relation between diffusion coefficient and viscosity,

$$D = \frac{k_B T}{6\pi\eta r} \ , \tag{11}$$

where k_B is Boltzmann's constant and r the hydrodynamic radius. If we assume r is mostly determined by the molecular size and not the charges, it is expected that a force field overestimating D will underestimate η. The default DME charges are larger in magnitude so it is expected D will be lower, as larger charges increase the activation energy for diffusive motion.[57] However, use of the default charges comes at the cost of overestimating the relative permittivity by a factor of two. This overestimation of permittivity may be related to an increased concentration of DME's most polar conformations, since liquids with larger molecular dipoles have higher permittivity.[46] It is known that the TraPPE model of DME does not reproduce its conformer populations very accurately[66,92] (please note, Ref. 92 has a published correction). In particular, TraPPE overestimates the population of the TGG conformer which has the largest dipole.[36]

To address the potential issue of statistical error, we obtain the standard deviation (SD) of the density, surface tension and viscosity measurements from five independent simulations. For all molecules, the SD is less than 10%, with the SD being negligible for the density measurements. Hence, we conclude the extended united-atom TraPPE force field is suitable to describe the physical properties of solvents relevant to LIBs, especially in reproducing the transport properties of carbonates EC, PC and DMC. However, the relative permittivity of DMC and DEC could not be reproduced accurately with either force field (TraPPE and CHARMM).

Single Solvent and Salt Structure

Figure 3 demonstrates the equilibrium solvation structure of different single solvents with 1M $LiPF_6$ and their salt distribution. In Figure 3(a) and (b), after equilibration, the $LiPF_6$ ions are distributed quite uniformly in the high permittivity cyclic carbonates EC and PC. Despite having the lowest permittivity, DMC is found to distribute the salt more uniformly than DME, demonstrating the importance of the carbonyl oxygen in solvating small cations. In Figure 3(g), the Li^+ and PF_6^- ions solvated by DMC are found to join together to form long chains of alternating positive and negative ions.

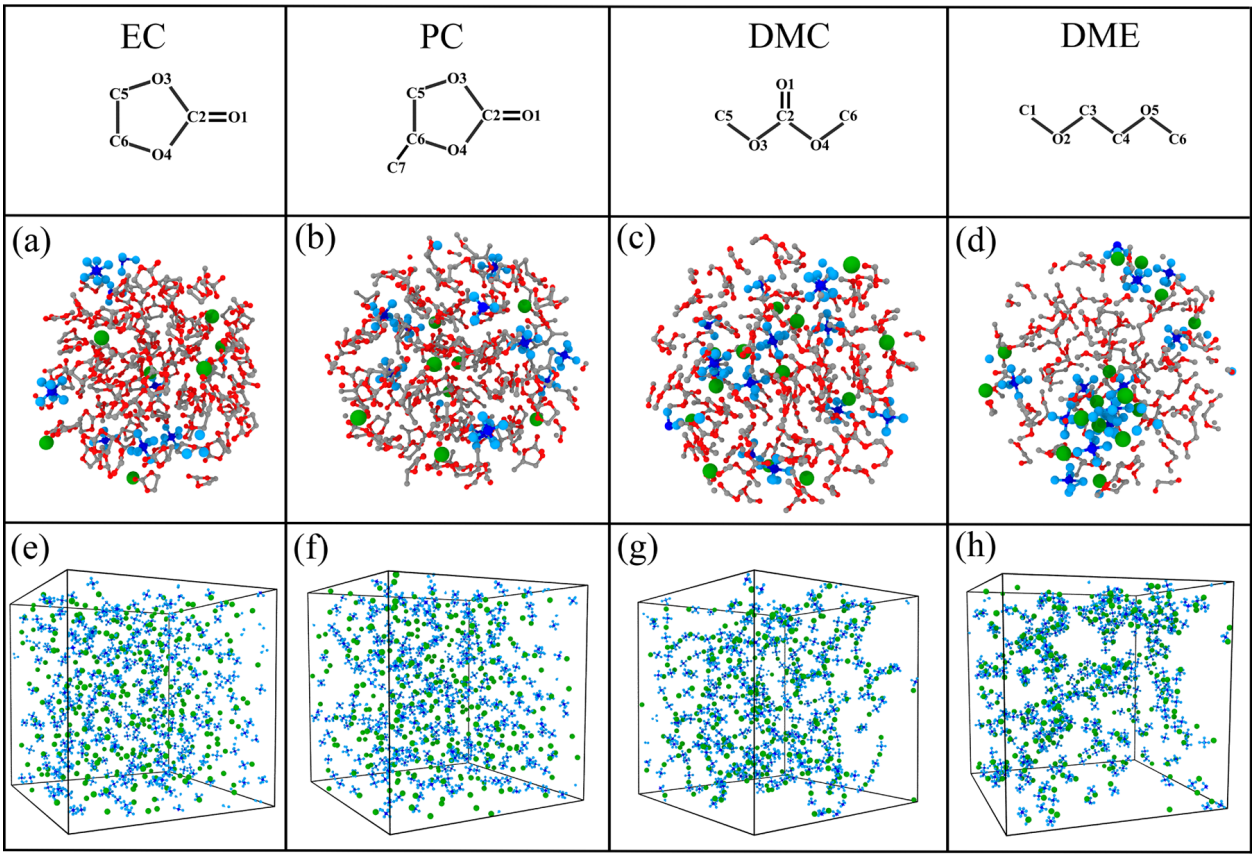

Figure 3: The final solvation structure and salt distribution of different single solvents with 1M $LiPF_6$ salt at 298 K, visualized using OVITO.[93] (a) structure of EC with $LiPF_6$; (b) structure of PC with $LiPF_6$; (c) structure of DMC with $LiPF_6$; (d) structure of DME with $LiPF_6$; (e) distribution of $LiPF_6$ in EC solvent; (f) distribution of $LiPF_6$ in PC solvent; (g) distribution of $LiPF_6$ in DMC solvent; (h) distribution of $LiPF_6$ in DME solvent. The red, grey, green and blue spheres represent O, C, Li^+ and PF_6^- atoms, respectively.

These differences in structure can be quantified using the RDF, g(r), which describes radial fluctuations in the density around a given central atom. This is used to measure the coordination number of various pairs of atoms or molecules, such as the average number of PF_6^- anions surrounding each Li^+. We analyzed the RDF of Li^+ ions with the neighboring atoms, O1 (carbonyl oxygen), Li^+ and P, with the results presented in Figure 4. The RDFs were calculated and time-averaged over the entire 12 ns trajectory which contains 3000 frames. There is a large peak located at ≈ 0.25 nm in g(r) of Li^+ with the double bonded O1 in EC/PC/DMC solvents, indicating that there is a high density of carbonyl oxygens surrounding Li^+ ions. Meanwhile, a smaller equivalent peak appears in the g(r) of Li^+ with O atoms in DME solvent. In the saline DME system, there is a strong peak in the RDFs of Li^+ ions with both P and Li^+ atoms at $r \approx 0.4$ nm and 0.5 nm respectively. This demonstrates incomplete dissolution of $LiPF_6$, consistent with the cluster structures observed in Figure 3(h). Comparing Figure 4(c) and (d), the first peak in the Li-P RDF is far larger in DMC/DME than EC/PC.

Then, we visualize the solvation shell around a Li^+ ion in different solvents and compute the corresponding coordination number in Figure 5. EC and PC are highly polar and the negatively charged carbonyl oxygen (O1) is located at the narrow pointed end of the molecule, which results in EC and PC forming a more complete solvation shell around Li^+ than DMC and DME. We also integrate their corresponding RDF from 0 to 0.45 nm to derive the coordination number for Li-O (lithium-solvent) and Li-P (lithium-anion) pairs, with the results (also in Fig. 5) consistent with the visualized configurations. For EC and PC, the number of O1 atoms in the Li^+ solvation shell are both approximately 6, whereas the number of O atoms surrounding Li^+ in DMC and DME solvents are about 4 and 2, respectively. There is negligible PF_6^- located in the first solvation shell of Li^+ in EC and PC solvent, which agrees well with the Li^+-EC coordination number of 5.69 obtained by an NMR study of 1M $LiPF_6$ in pure EC solvent.[94] In the saline DMC and DME systems, on the other hand, there are 1.8 and 2.1 PF_6^- cations around the Li^+ ions, respectively.

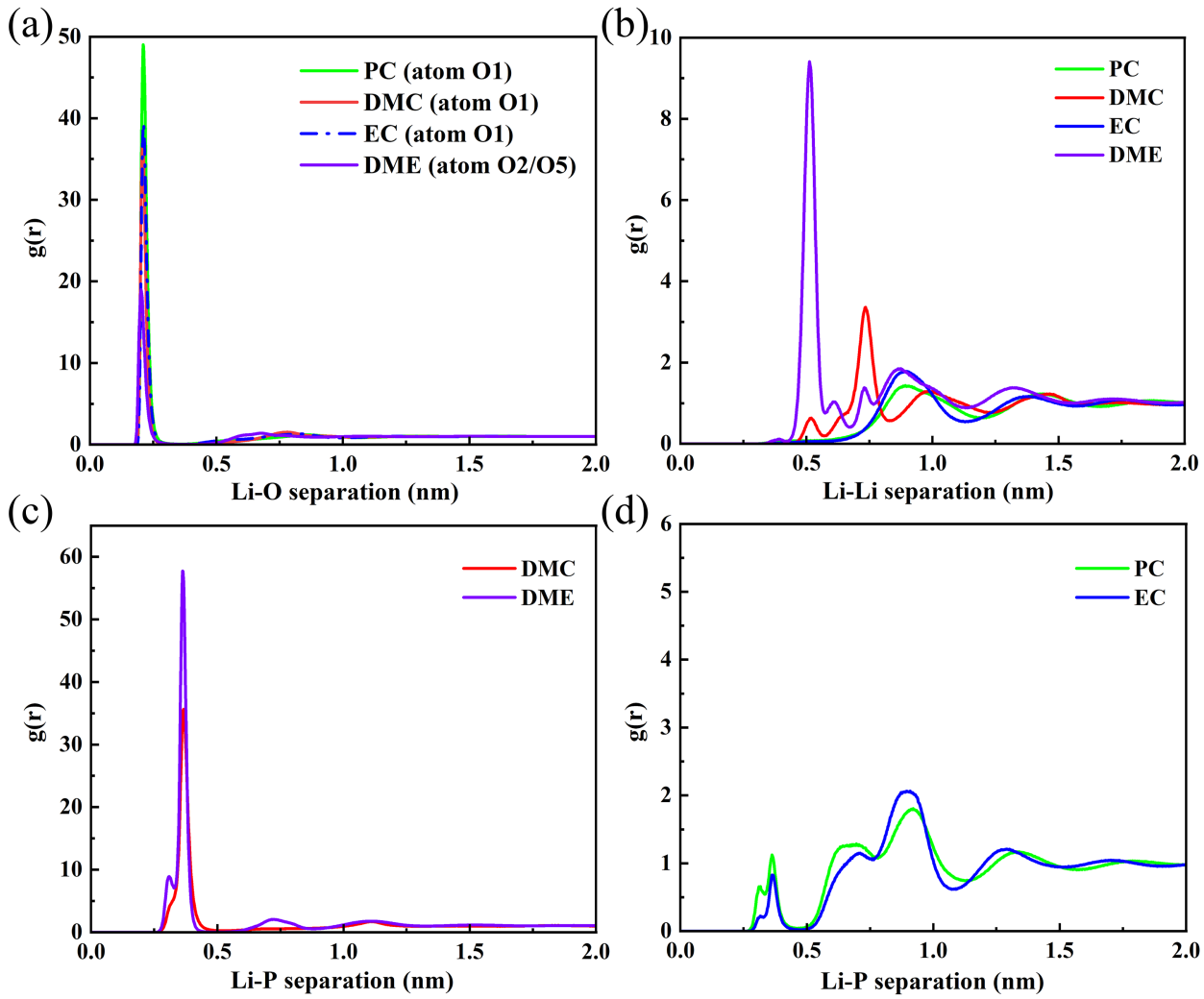

Figure 4: The RDF of Li^+ atoms with their surrounding O, Li^+ and P atoms when dissolved in EC, PC, DME and DMC pure solvents. (a) RDF of Li-O; (b) RDF of Li-Li; (c) RDF of Li-P with DMC and DME solvents; (d) RDF of Li-P with EC and PC solvents, all measured at 298 K.

	EC	PC	DMC	DME
coordination configurations	(a) 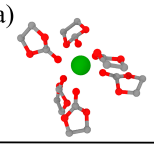	(b) 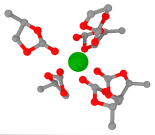	(c) 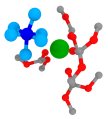	(d) 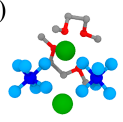
coordination number	Li-O1 5.98 Li-P 0.04	Li-O1 5.78 Li-P 0.07	Li-O1 3.93 Li-P 1.66	Li-O2/O5 1.82 Li-P 2.06

Figure 5: Visualization of nearest-neighbor solvation shells around a Li^+ ion in solvents (a) EC; (b) PC; (c) DMC; (d) DME. Coordination numbers for Li-O and Li-P pairs at 298 K are derived from integration of the corresponding RDF using a cutoff of 4.5 Å.

Mixed Solvent Physical Properties

We perform simulations using the extended TraPPE force field to measure self-diffusion coefficients and relative permittivities for relevant binary electrolytes (EC-DMC, PC-DMC) with varying volume fractions. Figure 6 (a) and (d) show that, as the EC or PC volume fraction is increased, the self-diffusion coefficient of all solvent molecules decreases sharply. After adding 1M $LiPF_6$ salt, the self-diffusion coefficient of all electrolytes is reduced by $> 50\%$, but the trend of the self-diffusion coefficient with EC/PC concentration stays the same for every component. The self-diffusion coefficients of PC and EC are always less than DMC in the solvent mixture with 1M $LiPF_6$. Since Li^+ is the slowest diffusing species, this may indicate a greater fraction of EC and PC molecules are bound to Li^+ as expected from the coordination analysis. In pure DMC, we see the diffusion coefficients of Li^+ and PF_6^- are nearly identical. This corresponds with the chain-like structures in Figure 3 (g), in which most ions are bound to counterions and therefore diffuse at the same speed. Unlike Li^+ and the solvent molecules, the diffusion coefficient of PF_6^- does not decrease monotonically as the EC or PC volume fractions are increased.

Compared to the all-atom MD and experimental data of Takeuchi *et al.*[54] for 1M $LiPF_6$ in PC, the TraPPE results represent an improvement on their MD results which underestimate diffusion coefficients by a larger factor. However, as the diffusion coefficient is still too low, we investigate the uniform charge-rescaling approach applied by Chaban[57] to ionic liquids. In this approach, the point charges of Li^+ and PF_6^- atoms are rescaled by a constant factor which is optimized to reproduce transport properties.

Figure 7 shows the dependence of the diffusion coefficients on the charge rescaling factor, finding a very strong dependence and suggesting an optimal factor of $\approx 85\%$. The error compared to experimental data[54] is -0.39%, 2.21% and -5.67% for PC, Li^+ and PF_6^- respectively. We also find the TraPPE model reproduces the ratio of the diffusion coefficients for the different molecules very well, with PF_6^- being slightly lower than PC, and Li^+ approximately half. At 85% charge rescaling, the Li^+-O1 coordination number is reduced from 5.78

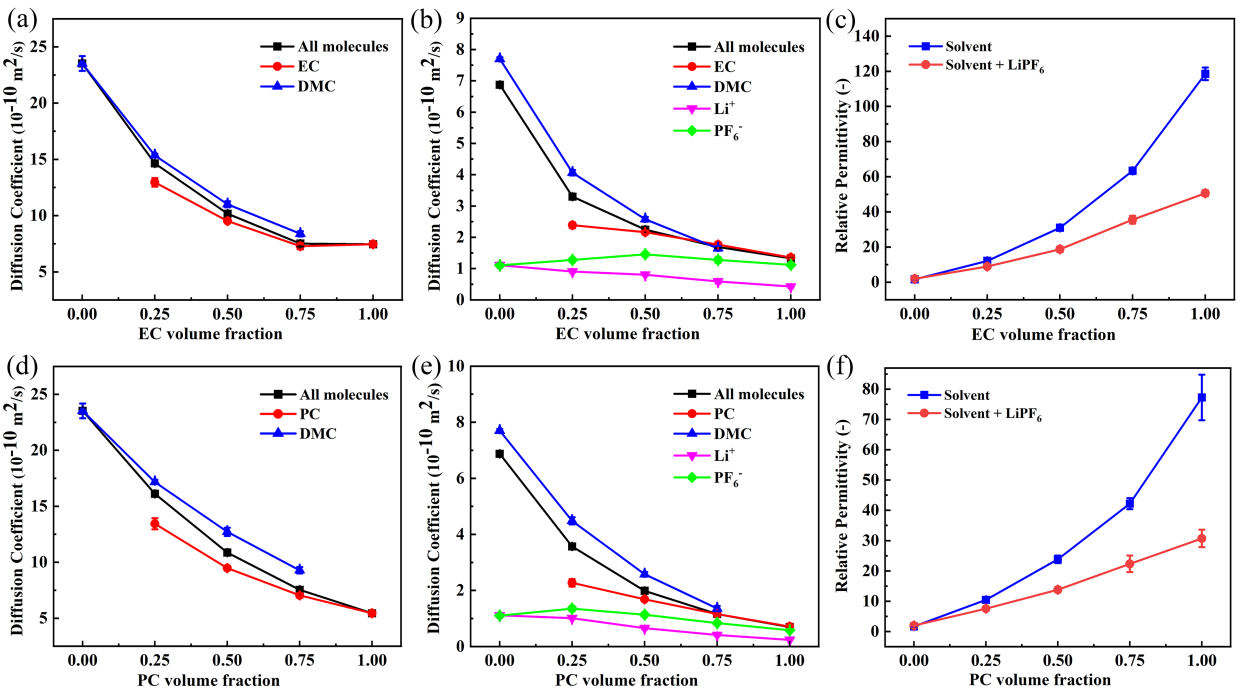

Figure 6: Computed diffusion coefficient and relative permittivity of binary solvent mixtures, some with 1M $LiPF_6$ (298 K). (a) diffusion coefficient of EC-DMC solvent mixture without salt; (b) diffusion coefficient of EC-DMC solvent mixture with 1M $LiPF_6$; (c) permittivity of EC-DMC solvent mixture both with and without salt; (d) diffusion coefficient of PC-DMC solvent mixture without salt; (e) diffusion coefficient of PC-DMC solvent mixture with 1M $LiPF_6$; (f) permittivity of PC-DMC solvent mixture both with and without salt.

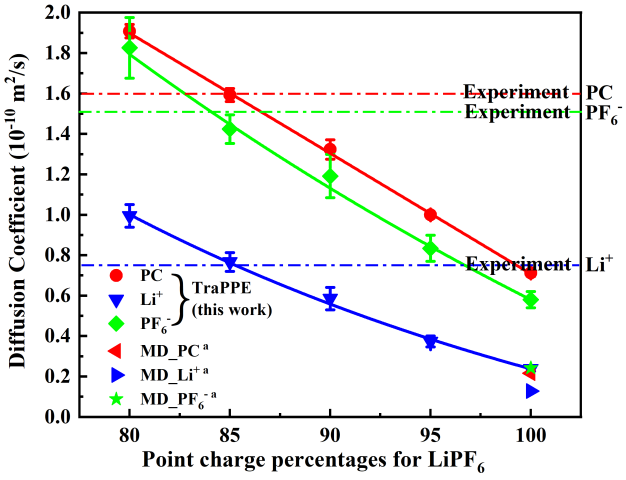

Figure 7: Diffusion coefficients of Li^+, PF_6^- and PC for 1M $LiPF_6$ in PC system (298 K). Charges of Li^+ and PF_6^- atoms are rescaled by factors from 80% to 100% (x axis). Experimental results are from Takeuchi *et al.*[54] [a]All-atom MD results also from Ref.[54]

(Fig. 5) to 5.13, which more closely aligns with values of ≈ 4.5 obtained from some neutron diffraction[17] and NMR diffusion[22] measurements.

Additionally, simulations using an 85% $LiPF_6$ charge rescaling factor were performed for a mixed electrolyte with EC:DMC at 50:50 wt% and 1M $LiPF_6$, with the computed diffusion coefficients given in Table S7 alongside comparable values computed by Borodin & Smith[95] (298 K). We find a ratio of Li^+ to PF_6^- diffusion coefficients of $D_{\mathrm{Li}}/D_{\mathrm{PF6}} = 0.60$. Hayamizu[21] found this ratio to be 0.57 for a similar electrolyte containing EC:DEC at 6:4 molar ratio and 1M $LiPF_6$ at 293 K (and a ratio of 0.59 at 303 K).

The trends of the EC-DMC and PC-DMC mixture permittivities are consistent with the saline ones—all permittivities are observed to increase as the EC and PC volume fraction is increased. Adding salt to systems with at least 25% EC or PC reduces their permittivity, a behavior which has also been observed and studied in saline water.[96]

The RDF of the Li^+ atoms with their surrounding O, Li^+ and P atoms in mixed solvent (EC-DMC) is shown in Figure 8 to demonstrate how the ratio of high and low permittivity solvents affects the salt dissociation. An interesting transition is observed between 0% and 25% EC by volume, as the structure of the short-ranged part of the Li-Li RDF changes completely such that the first two peaks are no longer present at 25% EC and above. This corresponds to a break down of the ordered chain-like structures of the salt in pure DMC solvent seen in Fig. 3(g). As the EC volume percentage is increased to 100%, EC forms a complete solvation shell around the Li^+ ions and therefore the peak of the Li-P RDF at 0.4 nm decreases close to zero.

Finally, we comment on the performance of the united-atom TraPPE model compared to a comparable all-atom model, in this case CHARMM. The improvement will depend primarily on the proportion of hydrogen atoms and choice of time step. When using a 1 fs time step, such as in Ref.,[48,97] the relative performance of TraPPE (which uses a 2 fs time step) averaged over EC, PC, DMC and DME simulations was found to be 3.6 times faster. However, commonly used techniques such as constraining C-H bonds to remove high-

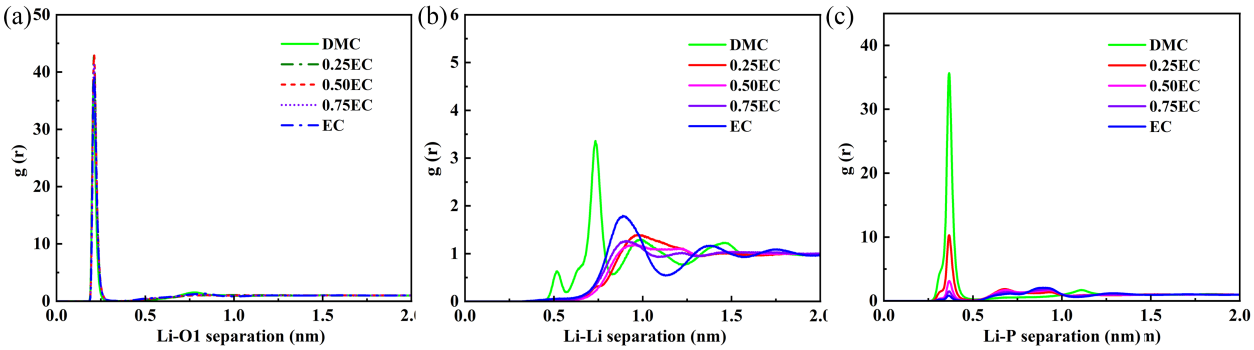

Figure 8: The RDF, g(r), of Li^+ ions with their surrounding O, Li^+ and P atoms for varying EC volume fraction in the EC-DMC binary mixture with 1M $LiPF_6$ at 298 K. (a) Li-O; (b) Li-Li; (c) Li-P.

frequency motion allow the time step of all-atom simulations to be increased to 2 fs, in which case the speedup factor is 1.8.

Conclusion

In this work, we have developed an extension to the TraPPE united-atom force field, compatible with widely used MD simulation codes including GROMACS, addressing the lack of efficient united-atom models validated for electrolyte solvents. This enables us to calculate important properties of electrolytes, such as self-diffusion coefficients, relative permittivity, surface tension and viscosity more efficiently. A systematic procedure for computing the properties of binary electrolytes as a function of solvent composition is applied, enabling optimization of electrolyte formulations for utilization in electrochemical devices. We demonstrate how the transport properties of the electrolyte solution, comprised of $LiPF_6$ salt and a binary mixture of two solvents, depends on the ratio of high and low permittivity solvents. Our results show that the $LiPF_6$ salt is dispersed uniformly in pure EC and PC solvents, and in both cases we observe the formation of complete solvation shells around the Li^+ ions, with six solvent molecules packed tightly. In contrast, $LiPF_6$ in DMC formed linear chains of alternating charge ions, and in DME solvent the salt formed globular clusters. Finally, we find the Li^+ and PF_6^- diffusion coefficients are nearly identical in pure DMC solvent,

but deviate as EC is added, with the Li^+ diffusion coefficient decreasing monotonically with increasing EC concentration.

Acknowledgement

We are grateful to the UK Materials and Molecular Modelling Hub for computational resources, which is partially funded by EPSRC (EP/P020194/1 and EP/T022213/1), as well as for the EPSRC Fellowship No. EP/R028915/1. We also acknowledge the financial support from the Natural Science Foundation of Shaanxi Province for the key project (2021JZ-07), and the Polymer Electromagnetic Functional Materials Innovation Team of Shaanxi Sanqin Scholars. We also thank Prof. Fernando Bresme of Imperial College London for helpful discussions during the inception of this work.

Supporting Information Available

Description of dihedral potential optimization. Archive containing GROMACS force field implementation, with the online repository github.com/SB8/trappe-electrolyte also provided. Supplementary Figures: Plots of dihedral potential energy surfaces; dependence of viscosity on cosine-acceleration parameter; DMC conformer equilibration; optimized charges vs r_p parameter; dependence of diffusion coefficient and permittivity on r_p. Supplementary Tables: $LiPF_6$ LJ parameters; solvent LJ parameters in TraPPE units (Å and K); force field parameters and computed properties for CHARMM; number of molecules in simulated systems; diffusion coefficients of EC:DMC electrolyte with ion charge rescaling.

References

(1) Xie, J.; Lu, Y.-C. A retrospective on lithium-ion batteries. *Nature Communications* **2020**, *11*, 1–4.

(2) Quartarone, E.; Mustarelli, P. Emerging trends in the design of electrolytes for lithium and post-lithium batteries. *Journal of The Electrochemical Society* **2020**, *167*, 050508.

(3) Goodenough, J. B.; Kim, Y. Challenges for rechargeable Li batteries. *Chemistry of Materials* **2010**, *22*, 587–603.

(4) Liang, Y.; Zhao, C.-Z.; Yuan, H.; Chen, Y.; Zhang, W.; Huang, J.-Q.; Yu, D.; Liu, Y.; Titirici, M.-M.; Chueh, Y.-L. et al. A review of rechargeable batteries for portable electronic devices. *InfoMat* **2019**, *1*, 6–32.

(5) Wang, Y.; Diaz, D. F. R.; Chen, K. S.; Wang, Z.; Adroher, X. C. Materials, technological status, and fundamentals of PEM fuel cells–a review. *Materials Today* **2020**, *32*, 178–203.

(6) Xiong, S.; Ji, J.; Ma, X. Environmental and economic evaluation of remanufacturing lithium-ion batteries from electric vehicles. *Waste Management* **2020**, *102*, 579–586.

(7) Masias, A.; Marcicki, J.; Paxton, W. A. Opportunities and challenges of lithium ion batteries in automotive applications. *ACS Energy Letters* **2021**, *6*, 621–630.

(8) Pagliaro, M. Renewable energy systems: Enhanced resilience, lower costs. *Energy Technology* **2019**, *7*, 1900791.

(9) Vimmerstedt, L.; Akar, S.; Mirletz, B.; Sekar, A.; Stright, D.; Augustine, C.; Beiter, P.; Bhaskar, P.; Blair, N.; Cohen, S. et al. *Annual Technology Baseline: The 2022 Electricity Update*; 2022.

(10) Huan, L.; Xie, J.; Chen, M.; Diao, G.; Zhao, R.; Zuo, T. Theoretical investigation of pillar[4]quinone as a cathode active material for lithium-ion batteries. *Journal of Molecular Modeling* **2017**, *23*, 1–9.

(11) Lanjan, A.; Choobar, B. G.; Amjad-Iranagh, S. Promoting lithium-ion battery performance by application of crystalline cathodes $Li_xMn_{1-z}Fe_zPO_4$. *Journal of Solid State Electrochemistry* **2020**, *24*, 157–171.

(12) Lanjan, A.; Choobar, B. G.; Amjad-Iranagh, S. First principle study on the application of crystalline cathodes $Li_2Mn_{0.5}TM_{0.5}O_3$ for promoting the performance of lithium-ion batteries. *Computational Materials Science* **2020**, *173*, 109417.

(13) Li, M.; Wang, C.; Chen, Z.; Xu, K.; Lu, J. New concepts in electrolytes. *Chemical Reviews* **2020**, *120*, 6783–6819.

(14) Van der Ven, A.; Deng, Z.; Banerjee, S.; Ong, S. P. Rechargeable alkali-ion battery materials: theory and computation. *Chemical Reviews* **2020**, *120*, 6977–7019.

(15) Franco, A. A.; Rucci, A.; Brandell, D.; Frayret, C.; Gaberscek, M.; Jankowski, P.; Johansson, P. Boosting rechargeable batteries R&D by multiscale modeling: myth or reality? *Chemical Reviews* **2019**, *119*, 4569–4627.

(16) Moon, H.; Mandai, T.; Tatara, R.; Ueno, K.; Yamazaki, A.; Yoshida, K.; Seki, S.; Dokko, K.; Watanabe, M. Solvent activity in electrolyte solutions controls electrochemical reactions in Li-ion and Li-sulfur batteries. *The Journal of Physical Chemistry C* **2015**, *119*, 3957–3970.

(17) Kameda, Y.; Umebayashi, Y.; Takeuchi, M.; Wahab, M. A.; Fukuda, S.; Ishiguro, S.-i.; Sasaki, M.; Amo, Y.; Usuki, T. Solvation structure of Li+ in concentrated LiPF6-propylene carbonate solutions. *The Journal of Physical Chemistry B* **2007**, *111*, 6104–6109.

(18) Maeda, S.; Kameda, Y.; Amo, Y.; Usuki, T.; Ikeda, K.; Otomo, T.; Yanagisawa, M.; Seki, S.; Arai, N.; Watanabe, H. et al. Local structure of Li^+ in concentrated ethylene carbonate solutions studied by low-frequency raman scattering and neutron diffraction

with $^{6}Li/^{7}Li$ isotopic substitution methods. *The Journal of Physical Chemistry B* **2017**, *121*, 10979–10987.

(19) Cazzanelli, E.; Mustarelli, P.; Benevelli, F.; Appetecchi, G. B.; Croce, F. Raman and NMR analysis of $LiClO_4$ concentrated solutions in ethylene carbonate-propylene carbonate. *Solid State Ionics* **1996**, *86*, 379–384.

(20) Hayamizu, K.; Aihara, Y.; Arai, S.; Martinez, C. G. Pulse-gradient spin-echo ^{1}H, ^{7}Li, and ^{19}F NMR diffusion and ionic conductivity measurements of 14 organic electrolytes containing LiN $(SO_2CF_3)_2$. *The Journal of Physical Chemistry B* **1999**, *103*, 519–524.

(21) Hayamizu, K. Temperature dependence of self-diffusion coefficients of ions and solvents in ethylene carbonate, propylene carbonate, and diethyl carbonate single solutions and ethylene carbonate+ diethyl carbonate binary solutions of LiPF6 studied by NMR. *Journal of Chemical & Engineering Data* **2012**, *57*, 2012–2017.

(22) Kondo, K.; Sano, M.; Hiwara, A.; Omi, T.; Fujita, M.; Kuwae, A.; Iida, M.; Mogi, K.; Yokoyama, H. Conductivity and solvation of Li+ ions of LiPF6 in propylene carbonate solutions. *The Journal of Physical Chemistry B* **2000**, *104*, 5040–5044.

(23) Feng, Z.; Higa, K.; Han, K. S.; Srinivasan, V. Evaluating transport properties and ionic dissociation of LiPF6 in concentrated electrolyte. *Journal of the Electrochemical Society* **2017**, *164*, A2434.

(24) Hwang, S.; Kim, D.-H.; Shin, J. H.; Jang, J. E.; Ahn, K. H.; Lee, C.; Lee, H. Ionic conduction and solution structure in LiPF6 and LiBF4 propylene carbonate electrolytes. *The Journal of Physical Chemistry C* **2018**, *122*, 19438–19446.

(25) Zhao, J.; Wang, L.; He, X.; Wan, C.; Jiang, C. Determination of lithium-ion transference numbers in LiPF6–PC solutions based on electrochemical polarization and NMR measurements. *Journal of The Electrochemical Society* **2008**, *155*, A292.

(26) Karatrantos, A.; Khan, M. S.; Yan, C.; Dieden, R.; Urita, K.; Ohba, T.; Cai, Q. Ion Transport in Organic Electrolyte Solutions for Lithium-ion Batteries and Beyond. *Journal of Energy and Power Technology* **2021**, *3*, 1–1.

(27) Allen, J. L.; Borodin, O.; Seo, D. M.; Henderson, W. A. Combined quantum chemical/Raman spectroscopic analyses of Li^+ cation solvation: Cyclic carbonate solvents-ethylene carbonate and propylene carbonate. *Journal of Power Sources* **2014**, *267*, 821–830.

(28) Cresce, A. V.; Russell, S. M.; Borodin, O.; Allen, J. A.; Schroeder, M. A.; Dai, M.; Peng, J.; Gobet, M. P.; Greenbaum, S. G.; Rogers, R. E. et al. Solvation behavior of carbonate-based electrolytes in sodium ion batteries. *Physical Chemistry Chemical Physics* **2017**, *19*, 574–586.

(29) Borodin, O.; Olguin, M.; Ganesh, P.; Kent, P. R.; Allen, J. L.; Henderson, W. A. Competitive lithium solvation of linear and cyclic carbonates from quantum chemistry. *Physical Chemistry Chemical Physics* **2016**, *18*, 164–175.

(30) Ong, M. T.; Verners, O.; Draeger, E. W.; Van Duin, A. C.; Lordi, V.; Pask, J. E. Lithium ion solvation and diffusion in bulk organic electrolytes from first-principles and classical reactive molecular dynamics. *The Journal of Physical Chemistry B* **2015**, *119*, 1535–1545.

(31) Pham, T. A.; Kweon, K. E.; Samanta, A.; Lordi, V.; Pask, J. E. Solvation and dynamics of sodium and potassium in ethylene carbonate from ab initio molecular dynamics simulations. *The Journal of Physical Chemistry C* **2017**, *121*, 21913–21920.

(32) Chang, T.-M.; Dang, L. X. Li^+ solvation and kinetics of Li^+–BF_4^-/PF_6^- ion pairs in ethylene carbonate. A molecular dynamics study with classical rate theories. *The Journal of Chemical Physics* **2017**, *147*, 161709.

(33) Zhang, X.; Kuroda, D. G. An ab initio molecular dynamics study of the solvation structure and ultrafast dynamics of lithium salts in organic carbonates: A comparison between linear and cyclic carbonates. *The Journal of Chemical Physics* **2019**, *150*, 184501.

(34) Karatrantos, A. V.; Ohba, T.; Cai, Q. Diffusion of ions and solvent in propylene carbonate solutions for lithium-ion battery applications. *Journal of Molecular Liquids* **2020**, *320*, 114351.

(35) Larkin, P. *Infrared and Raman spectroscopy: principles and spectral interpretation*; Elsevier, 2017.

(36) Goutev, N.; Ohno, K.; Matsuura, H. Raman spectroscopic study on the conformation of 1,2-dimethoxyethane in the liquid phase and in aqueous solutions. *The Journal of Physical Chemistry A* **2000**, *104*, 9226–9232.

(37) Wada, R.; Fujimoto, K.; Kato, M. Why is poly (oxyethylene) soluble in water? Evidence from the thermodynamic profile of the conformational equilibria of 1,2-dimethoxyethane and dimethoxymethane revealed by Raman Spectroscopy. *The Journal of Physical Chemistry B* **2014**, *118*, 12223–12231.

(38) Yeh, I.-C.; Hummer, G. System-size dependence of diffusion coefficients and viscosities from molecular dynamics simulations with periodic boundary conditions. *The Journal of Physical Chemistry B* **2004**, *108*, 15873–15879.

(39) Yaakov, D.; Gofer, Y.; Aurbach, D.; Halalay, I. C. On the study of electrolyte solutions for Li-ion batteries that can work over a wide temperature range. *Journal of the Electrochemical Society* **2010**, *157*, A1383.

(40) Li, Z.; Bommier, C.; Chong, Z. S.; Jian, Z.; Surta, T. W.; Wang, X.; Xing, Z.; Neuefeind, J. C.; Stickle, W. F.; Dolgos, M. et al. Mechanism of Na-Ion storage in hard

carbon anodes revealed by heteroatom doping. *Advanced Energy Materials* **2017**, *7*, 1602894.

(41) Eshetu, G. G.; Grugeon, S.; Laruelle, S.; Boyanov, S.; Lecocq, A.; Bertrand, J.-P.; Marlair, G. In-depth safety-focused analysis of solvents used in electrolytes for large scale lithium ion batteries. *Physical Chemistry Chemical Physics* **2013**, *15*, 9145–9155.

(42) Chernyak, Y. Dielectric constant, dipole moment, and solubility parameters of some cyclic acid esters. *Journal of Chemical & Engineering Data* **2006**, *51*, 416–418.

(43) Payne, R.; Theodorou, I. E. Dielectric properties and relaxation in ethylene carbonate and propylene carbonate. *The Journal of Physical Chemistry* **1972**, *76*, 2892–2900.

(44) Zhang, S.; Jow, T.; Amine, K.; Henriksen, G. $LiPF_6$–EC–EMC electrolyte for Li-ion battery. *Journal of Power Sources* **2002**, *107*, 18–23.

(45) Valøen, L. O.; Reimers, J. N. Transport properties of $LiPF_6$-based Li-ion battery electrolytes. *Journal of The Electrochemical Society* **2005**, *152*, A882.

(46) Xu, K. Nonaqueous liquid electrolytes for lithium-based rechargeable batteries. *Chemical Reviews* **2004**, *104*, 4303–4418.

(47) Jorgensen, W. L.; Maxwell, D. S.; Tirado-Rives, J. Development and testing of the OPLS all-atom force field on conformational energetics and properties of organic liquids. *Journal of the American Chemical Society* **1996**, *118*, 11225–11236.

(48) You, X.; Chaudhari, M. I.; Rempe, S. B.; Pratt, L. R. Dielectric relaxation of ethylene carbonate and propylene carbonate from molecular dynamics simulations. *The Journal of Physical Chemistry B* **2016**, *120*, 1849–1853.

(49) MacKerell Jr, A. D.; Brooks, B.; Brooks III, C. L.; Nilsson, L.; Roux, B.; Won, Y.; Karplus, M. CHARMM: the energy function and its parameterization. *Encyclopedia of Computational Chemistry* **2002**, *1*.

(50) Brooks, B. R.; Brooks III, C. L.; Mackerell Jr, A. D.; Nilsson, L.; Petrella, R. J.; Roux, B.; Won, Y.; Archontis, G.; Bartels, C.; Boresch, S. et al. CHARMM: the biomolecular simulation program. *Journal of Computational Chemistry* **2009**, *30*, 1545–1614.

(51) Zoete, V.; Cuendet, M. A.; Grosdidier, A.; Michielin, O. SwissParam: A fast force field generation tool for small organic molecules. *Journal of Computational Chemistry* **2011**, *32*, 2359–2368.

(52) Caleman, C.; Van Maaren, P. J.; Hong, M.; Hub, J. S.; Costa, L. T.; Van Der Spoel, D. Force field benchmark of organic liquids: density, enthalpy of vaporization, heat capacities, surface tension, isothermal compressibility, volumetric expansion coefficient, and dielectric constant. *Journal of Chemical Theory and Computation* **2012**, *8*, 61–74.

(53) Núñez Rojas, E.; Aguilar-Pineda, J. A.; Pérez de la Luz, A.; de Jesús González, E. N.; Alejandre, J. Force field benchmark of the TraPPE-UA for polar liquids: density, heat of vaporization, dielectric constant, surface tension, volumetric expansion coefficient, and isothermal compressibility. *The Journal of Physical Chemistry B* **2018**, *122*, 1669–1678.

(54) Takeuchi, M.; Kameda, Y.; Umebayashi, Y.; Ogawa, S.; Sonoda, T.; Ishiguro, S.-i.; Fujita, M.; Sano, M. Ion–ion interactions of $LiPF_6$ and $LiBF_4$ in propylene carbonate solutions. *Journal of Molecular Liquids* **2009**, *148*, 99–108.

(55) Borodin, O.; Smith, G. D. Development of many- body polarizable force fields for Li-battery components: 1. Ether, Alkane, and carbonate-based solvents. *The Journal of Physical Chemistry B* **2006**, *110*, 6279–6292.

(56) Chaudhari, M. I.; Nair, J. R.; Pratt, L. R.; Soto, F. A.; Balbuena, P. B.; Rempe, S. B. Scaling atomic partial charges of carbonate solvents for lithium ion solvation and diffusion. *Journal of Chemical Theory and Computation* **2016**, *12*, 5709–5718.

(57) Chaban, V. Polarizability versus mobility: atomistic force field for ionic liquids. *Physical Chemistry Chemical Physics* **2011**, *13*, 16055–16062.

(58) Van Gunsteren, W. F.; Berendsen, H. J. A leap-frog algorithm for stochastic dynamics. *Molecular Simulation* **1988**, *1*, 173–185.

(59) Berendsen, H. J.; van der Spoel, D.; van Drunen, R. GROMACS: a message-passing parallel molecular dynamics implementation. *Computer Physics Communications* **1995**, *91*, 43–56.

(60) Stubbs, J. M.; Potoff, J. J.; Siepmann, J. I. Transferable potentials for phase equilibria. 6. United-atom description for ethers, glycols, ketones, and aldehydes. *The Journal of Physical Chemistry B* **2004**, *108*, 17596–17605.

(61) Maerzke, K. A.; Schultz, N. E.; Ross, R. B.; Siepmann, J. I. TraPPE-UA force field for acrylates and Monte Carlo simulations for their mixtures with alkanes and alcohols. *The Journal of Physical Chemistry B* **2009**, *113*, 6415–6425.

(62) Keasler, S. J.; Charan, S. M.; Wick, C. D.; Economou, I. G.; Siepmann, J. I. Transferable potentials for phase equilibria–united atom description of five-and six-membered cyclic alkanes and ethers. *The Journal of Physical Chemistry B* **2012**, *116*, 11234–11246.

(63) Hess, B.; Bekker, H.; Berendsen, H. J.; Fraaije, J. G. LINCS: a linear constraint solver for molecular simulations. *Journal of Computational Chemistry* **1997**, *18*, 1463–1472.

(64) Kaminski, G. A.; Jorgensen, W. L. Host–guest chemistry of rotaxanes and catenanes: application of a polarizable all-atom force field to cyclobis (paraquat-p-phenylene) complexes with disubstituted benzenes and biphenyls. *Journal of the Chemical Society, Perkin Transactions 2* **1999**, 2365–2375.

(65) Canongia Lopes, J. N.; Deschamps, J.; Pádua, A. A. Modeling ionic liquids using a systematic all-atom force field. *The Journal of Physical Chemistry B* **2004**, *108*, 2038–2047.

(66) Burrows, S. A. Multiscale simulation of transport phenomena in semi-solid flow batteries. Ph.D. thesis, Imperial College London, 2017.

(67) Becke, A. D. Density-functional thermochemistry. III. The role of exact exchange. *The Journal of Chemical Physics* **1993**, *98*, 5648–5652.

(68) Lee, C.; Yang, W.; Parr, R. G. Development of the Colle-Salvetti correlation-energy formula into a functional of the electron density. *Physical Review B* **1988**, *37*, 785.

(69) Stephens, P. J.; Devlin, F. J.; Chabalowski, C. F.; Frisch, M. J. Ab initio calculation of vibrational absorption and circular dichroism spectra using density functional force fields. *The Journal of Physical Chemistry* **1994**, *98*, 11623–11627.

(70) Grimme, S.; Antony, J.; Ehrlich, S.; Krieg, H. A consistent and accurate ab initio parametrization of density functional dispersion correction (DFT-D) for the 94 elements H-Pu. *The Journal of Chemical Physics* **2010**, *132*, 154104.

(71) Dunning Jr, T. H. Gaussian basis sets for use in correlated molecular calculations. I. The atoms boron through neon and hydrogen. *The Journal of Chemical Physics* **1989**, *90*, 1007–1023.

(72) Kendall, R. A.; Dunning Jr, T. H.; Harrison, R. J. Electron affinities of the first-row atoms revisited. Systematic basis sets and wave functions. *The Journal of Chemical Physics* **1992**, *96*, 6796–6806.

(73) Valiev, M.; Bylaska, E. J.; Govind, N.; Kowalski, K.; Straatsma, T. P.; Van Dam, H. J.; Wang, D.; Nieplocha, J.; Apra, E.; Windus, T. L. et al. NWChem: A comprehensive and

scalable open-source solution for large scale molecular simulations. *Computer Physics Communications* **2010**, *181*, 1477–1489.

(74) Berendsen, H. J. C.; Postma, J. P. M.; van Gunsteren, W. F.; DiNola, A.; Haak, J. R. Molecular dynamics with coupling to an external bath. *The Journal of Chemical Physics* **1984**, *81*, 3684–3690.

(75) Parrinello, M.; Rahman, A. Polymorphic transitions in single crystals: A new molecular dynamics method. *Journal of Applied Physics* **1981**, *52*, 7182–7190.

(76) Bussi, G.; Donadio, D.; Parrinello, M. Canonical sampling through velocity rescaling. *The Journal of Chemical Physics* **2007**, *126*, 014101.

(77) Gereben, O.; Pusztai, L. On the accurate calculation of the dielectric constant from molecular dynamics simulations: The case of SPC/E and SWM4-DP water. *Chemical Physics Letters* **2011**, *507*, 80–83.

(78) Neumann, M. The dielectric constant of water. Computer simulations with the MCY potential. *The Journal of Chemical Physics* **1985**, *82*, 5663–5672.

(79) Neumann, M. Dipole moment fluctuation formulas in computer simulations of polar systems. *Molecular Physics* **1983**, *50*, 841–858.

(80) Allen, M. P.; Tildesley, D. J. *Computer simulation of liquids*; Oxford University Press, 2017.

(81) Muller, E. A.; Ervik, Å.; Mejía, A. A guide to computing interfacial properties of fluids from molecular simulations [Article v1.0]. *Living Journal of Computational Molecular Science* **2020**, *2*, 21385–21385.

(82) Hess, B. Determining the shear viscosity of model liquids from molecular dynamics simulations. *The Journal of Chemical Physics* **2002**, *116*, 209–217.

(83) Bohets, H.; van der Veken, B. J. On the conformational behavior of dimethyl carbonate. *Physical Chemistry Chemical Physics* **1999**, *1*, 1817–1826.

(84) Reddy, S. K.; Balasubramanian, S. Liquid dimethyl carbonate: a quantum chemical and molecular dynamics study. *The Journal of Physical Chemistry B* **2012**, *116*, 14892–14902.

(85) Chen, Q. P.; Xie, S.; Foudazi, R.; Lodge, T. P.; Siepmann, J. I. Understanding the molecular weight dependence of χ and the effect of dispersity on polymer blend phase diagrams. *Macromolecules* **2018**, *51*, 3774–3787.

(86) Naejus, R.; Damas, C.; Lemordant, D.; Coudert, R.; Willmann, P. Excess thermodynamic properties of the ethylene carbonate–trifluoroethyl methyl carbonate and propylene carbonate–trifluoroethyl methyl carbonate systems at T=(298.15 or 315.15) K. *The Journal of Chemical Thermodynamics* **2002**, *34*, 795–806.

(87) Uchida, S.; Kiyobayashi, T. What differentiates the transport properties of lithium electrolyte in ethylene carbonate mixed with diethylcarbonate from those mixed with dimethylcarbonate? *Journal of Power Sources* **2021**, *511*, 230423.

(88) Wang, F.; Wu, J.; Liu, Z. Surface tensions of mixtures of diesel oil or gasoline and dimethoxymethane, dimethyl carbonate, or ethanol. *Energy & Fuels* **2006**, *20*, 2471–2474.

(89) Zhao, G.; Bi, S.; Li, X.; Wu, J. Surface tension of diethyl carbonate, 1,2-dimethoxyethane and diethyl adipate. *Fluid Phase Equilibria* **2010**, *295*, 46–49.

(90) Barthel, J.; Neueder, R.; Roch, H. Density, relative permittivity, and viscosity of propylene carbonate+ dimethoxyethane mixtures from 25° C to 125° C. *Journal of Chemical & Engineering Data* **2000**, *45*, 1007–1011.

(91) Zisman, W. A. *Relation of the equilibrium contact angle to liquid and solid constitution*; ACS Publications, 1964; Vol. 43; pp 1–51.

(92) Fischer, J.; Paschek, D.; Geiger, A.; Sadowski, G. Modeling of aqueous poly (oxyethylene) solutions: 1. Atomistic simulations. *The Journal of Physical Chemistry B* **2008**, *112*, 2388–2398.

(93) Stukowski, A. Visualization and analysis of atomistic simulation data with OVITO–the Open Visualization Tool. *Modelling and Simulation in Materials Science and Engineering* **2009**, *18*, 015012.

(94) Bogle, X.; Vazquez, R.; Greenbaum, S.; Cresce, A. v. W.; Xu, K. Understanding Li^+–solvent interaction in nonaqueous carbonate electrolytes with ^{17}O NMR. *The Journal of Physical Chemistry Letters* **2013**, *4*, 1664–1668.

(95) Borodin, O.; Smith, G. D. Quantum chemistry and molecular dynamics simulation study of dimethyl carbonate: ethylene carbonate electrolytes doped with $LiPF_6$. *The Journal of Physical Chemistry B* **2009**, *113*, 1763–1776.

(96) Hasted, J.; Ritson, D.; Collie, C. Dielectric properties of aqueous ionic solutions. Parts I and II. *The Journal of Chemical Physics* **1948**, *16*, 1–21.

(97) Lee, H.; Venable, R. M.; MacKerell Jr, A. D.; Pastor, R. W. Molecular dynamics studies of polyethylene oxide and polyethylene glycol: hydrodynamic radius and shape anisotropy. *Biophysical journal* **2008**, *95*, 1590–1599.

TOC Graphic

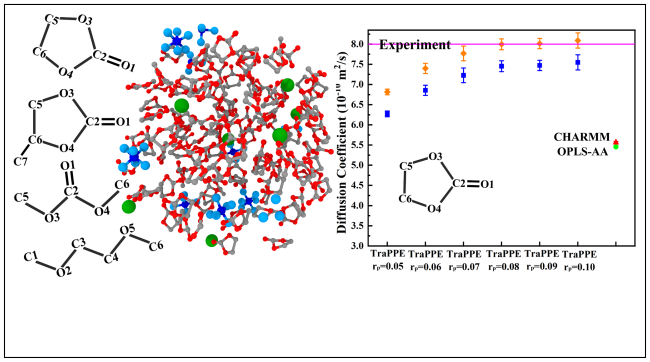
Experiment
CHARMM
OPLS-AA
Diffusion Coefficient (10^{-10} m^2/s)
TraPPE r_F=0.05
TraPPE r_F=0.06
TraPPE r_F=0.07
TraPPE r_F=0.08
TraPPE r_F=0.09
TraPPE r_F=0.10